



HAL
open science

Local organization of Fe³⁺ into nano-CeO₂ with controlled morphologies and its impact on reducibility properties

Iona Moog, Cédric Feral-Martin, Mathieu Duttine, Alain Wattiaux, Carmelo Prestipino, Santiago Figueroa, Jérôme Majimel, Alain Demourgues

► To cite this version:

Iona Moog, Cédric Feral-Martin, Mathieu Duttine, Alain Wattiaux, Carmelo Prestipino, et al.. Local organization of Fe³⁺ into nano-CeO₂ with controlled morphologies and its impact on reducibility properties. *Journal of Materials Chemistry A*, 2014, 2 (47), pp.20402-20414. 10.1039/C4TA02631D . hal-01082706

HAL Id: hal-01082706

<https://hal.science/hal-01082706>

Submitted on 28 Jun 2022

HAL is a multi-disciplinary open access archive for the deposit and dissemination of scientific research documents, whether they are published or not. The documents may come from teaching and research institutions in France or abroad, or from public or private research centers.

L'archive ouverte pluridisciplinaire **HAL**, est destinée au dépôt et à la diffusion de documents scientifiques de niveau recherche, publiés ou non, émanant des établissements d'enseignement et de recherche français ou étrangers, des laboratoires publics ou privés.

Local organization of Fe³⁺ into nano-CeO₂ with controlled morphologies and its impact on reducibility properties

Iona Moog,^a Cédric Feral-Martin,^a Mathieu Duttine,^a Alain Wattiaux,^a Carmelo Prestipino,^b Santiago Figueroa,^c

Jérôme Majimel^a and Alain Demourgues^{*a}

Ce and Fe are the main metal additives which have been tested by many laboratories for their catalytic activity at low temperature for soot oxidation in diesel engines. The key role and impact of Fe on the reducibility properties of ceria have been investigated on the basis of composition and structural features considering various synthesis routes. Two different procedures were used to prepare iron-substituted cerium dioxide Ce_{1-x}Fe_xO_{2-x/2}: a classical co-precipitation route followed by annealing at $T = 600$ °C and an unusual microwave-assisted hydrothermal synthesis at $T = 200$ °C. The highest surface areas around 100 m² g⁻¹, have been obtained for oxides containing the largest Fe amount and prepared by the microwave-assisted route. Solid solutions were obtained up to $x = 0.15$ and 0.20 through microwave-assisted and co-precipitation routes, respectively. The highest decrease of the lattice parameter is observed for compounds prepared by the microwave-assisted route. The TEM analysis reveals a nano-cubic shape (with mainly {001} planes) for compounds prepared by the microwave-assisted route and containing low Fe amount. For the other compounds prepared also by the co-precipitation process, a nano-polyhedron shape corresponding to a thermodynamically stable morphology is observed. EPR ($T = 5$ K, very low Fe rates), Mössbauer (room temperature, $x = 0.10$) and XANES-EXAFS (RT and $T = 20$ K) spectroscopies studies showed that Fe ions adopt the trivalent state and are located in isolated distorted (orthorhombic and axial distortions) octahedra or form Fe clusters. The local organization of Fe³⁺ plays a key role in the oxygen vacancy distribution and consequently the reducibility properties of the Ce_{1-x}Fe_xO_{2-x/2} solid solution. For the compounds prepared by the microwave-assisted route, a large proportion of Fe³⁺ is located in isolated distorted octahedral sites that contribute to affect a high number of Ce⁴⁺ nearest neighbors with a high mobility of oxygen vacancies. In this case, the oxygen vacancies are well distributed around Ce⁴⁺ and Fe³⁺. In the case of compounds obtained by the co-precipitation route, Fe clusters abundance is higher and consequently oxygen vacancies are mainly located around Fe clusters. Such a distribution should explain the lower solubility limit and the larger variation of the cell parameter *versus* x Fe content in the series prepared by the microwave-assisted route. It is shown that these last compounds exhibit better reducibility properties with a doubled reduction rate (comparison between $x(\text{Fe}) = 0.05$ and pure CeO₂) equal to 60% at $T = 550$ °C due to the iron local organization, a nano-cubic morphology and a higher surface area.

DOI: 10.1039/XXXXXXXXXX

^aCNRS, University of Bordeaux, ICMCB, UPR 9048, F-33600 Pessac, France. E-mail: demourg@icmcb-bordeaux.cnrs.fr

^bSciences chimiques de Rennes, UMR-CNRS 6226, Campus de Beaulieu, Bat 10B, 35042 Rennes, France

^cEuropean Synchrotron Radiation Facility, 6, rue Jules HOROWITZ, BP220, 38043 Grenoble, France

Introduction

Numerous studies have been devoted to ceria and related materials used as oxygen buffers in catalysts for removing hydrocarbons, carbon monoxide and nitrogen oxides from automobile exhausts.^{1,2} The creation of anionic vacancies into the fluorite-type networks are associated with the valence change of Ce between Ce⁴⁺(4f⁰) and Ce³⁺(4f¹). The rate of reduced cerium ions stabilized into the structure must be large and the reduction has to occur at low temperature. There are several driving concepts to increase the Ce reducibility or Ce³⁺ stabilization at low temperatures into the fluorite-type structures. The formation of high content of Ce³⁺ at low temperature

is possible when Ce^{4+} polyhedra are locally distorted, creating mainly $\text{Ce}^{4+}\text{-O}^{2-}$ ionic bonds. Then, the creation of oxygen vacancies and consequently oxygen diffusion becomes easier.

By playing with the structural features, the local environment of Ce can be modified by appropriate cation substitutions³ such as Zr^{4+} (ref. 4 and 5) or lanthanides Ln^{3+} (ref. 6–12) and lead to various crystallized networks and space groups related to the fluorite-type structure such as tetragonal fluorite (SG: $P4_2/nmc$),¹³ pyrochlore (SG: $Fd\bar{3}m$)⁵ or bixbyite (SG: $Ia\bar{3}$).¹⁴ Furthermore, appropriate cation substitutions without a structural change by keeping the fluorite network, allow for modification of redox properties.³ The competitive bonds around Ce^{4+} will play indeed a key role in this latter case.

Finally, high surface areas and various morphologies exposing various Ce/O reticular planes with different local environments, charges¹⁵ and atomic density allow for reaching highly reduced Ce rates at low temperatures. Theoretical calculations¹⁶ have shown that the formation energy of anion vacancies for various CeO_2 surfaces follows the order $\{110\} < \{100\} < \{111\}$. Hydrolysis of cerium salts combined with hydrothermal treatment allows for preparing single crystalline CeO_2 nano-polyhedra revealing $\{111\}$ and $\{100\}$ planes, nanocubes with $\{100\}$ planes, and nanorods with $\{111\}$ and $\{001\}$ planes.¹⁵ Then, because of these shapes and revealed reticular planes, the ability to release oxygen and the reducibility will change for the various geometries.

Hydrolysis and precipitation of Ce^{3+} salt in a basic medium followed by annealing at high temperatures,^{17,18} sol-gel methods¹⁹ and hydrothermal routes^{4,20} are the common processes to prepare high surface areas CeO_2 . Other rare earth metals or transition metals substituting Ce^{4+} are directly incorporated into the solutions containing different salts. The pH can be adjusted depending on the precipitation domain.

Most of rare earth ions, for instance from La^{3+} to Tb^{4+} (ref. 6–12), have been substituted for Ce^{4+} and anionic vacancies are stabilized into the fluorite network as trivalent rare earth ions are incorporated. The largest increase of the cell parameter is observed when La^{3+} (ref. 6 and 7) are substituted for Ce^{4+} despite the creation of oxygen vacancies. The cell parameter expansion decreases when Gd^{3+} ions¹¹ are incorporated in the fluorite network and it remains constant as Pr^{4+} or Tb^{4+} (ref. 7 and 12) are present. The ionic radius of rare earths governs the variation of the cell parameter. For other tetravalent cations such as Zr^{4+} (ref. 21) or Sn^{4+} ,²² derived structures from the fluorite-type network can be stabilized and the Ce reducibility is enhanced, thanks to a change in the local environment of Ce^{4+} .

For transition metals, substitution of Ce^{4+} ions and insertion into vacant sites of fluorite network can be considered. However, except for Zr^{4+} as well as Sn^{4+} ions whose ionic size is smaller than that of Ce^{4+} but higher than that of other 1st row transition metals, it is often very difficult to conclude about the solubility limit and the variation of the cell parameter. In the case of Ti^{4+} where an enhancement of reducibility properties has to be also noted,^{23,24} the cell parameter slightly decreased (from 5.41 to 5.39 Å) as a high content of Ti^{4+} equal to 40% is reached. An EXAFS study reveals the occurrence of a (4 + 4) local

environment of Ti^{4+} with Ti–O bond distances at 1.9 Å and 2.5 Å, respectively.²⁴ In the case of trivalent^{25,26} or divalent transition metals²⁷ substituted for Ce^{4+} , oxygen vacancies are stabilized due to charge electroneutrality.

To improve the oxidation rate of a diesel particulate matter at low temperatures, a combination of a particulate filter and a metal fuel additive is used nowadays in most of vehicles. Ce and Fe are the main metal additives which have been tested for their activity at low temperature for soot oxidation during the last 20 years. For Fe^{3+} ions, numerous studies mention the occurrence of substitution as well as insertion sites with distorted octahedral sites.^{17–20,28–34} Then the existence of defects $3\text{Fe}'_{\text{Ce}} : \text{Fe}_i''$ (in the Kröger–Vink notation) has been proposed³⁵ to explain the absence of oxygen vacancies revealed by the Raman study. If Fe^{3+} ions are incorporated into the cationic holes of the fluorite network, strong Ce–Fe interactions at around 2.7 Å appear and because of the reorganization of oxygen and vacancies, the occurrence of Fe insertion into fluorite is highly improbable whereas the Fe substitution for Ce^{4+} seems more evident. The highest Fe rate around 0.3 (ref. 36) has been stabilized into ceria and the cell parameter can decrease from 5.41 to 5.34 Å. Moreover, the Fe content and its oxidation state as well as the variation of the cell parameter strongly depend on the synthesis route.^{17–20,28–36} Some authors mentioned indeed the stabilization of $\text{Fe}^{2+}/\text{Fe}^{3+}$ valence states in doped- CeO_2 nanocrystals as well as the occurrence of oxygen vacancies revealed by Raman spectroscopy.^{37,38} In addition, many controversies exist about the local environment of Fe^{3+} into ceria as well as the variations of cell parameter and the solubility limit. Finally, the relationships between composition, structural features and Ce reducibility must be explained.

This paper aims to investigate the structural features of $\text{Ce}_{1-x}\text{Fe}_x\text{O}_{2-x/2}$ solid solutions and the impact on reducibility properties. Two different routes, the co-precipitation method (CP) followed by annealing at $T = 600$ °C and the microwave-assisted process (MW) were used to obtain the $\text{Ce}_{1-x}\text{Fe}_x\text{O}_{2-x/2}$ solid solution. The microwave-assisted synthesis is an interesting route because of the short reaction time, the homogeneous temperature³⁹ and the absence of further heat treatment. It is interesting to compare both these synthesis routes, because the kinetics of reactions and the way to incorporate Fe into ceria are clearly different. Furthermore the morphologies of the nanoparticles as well as the surface areas will not be the same.

In this study, structural characterizations have been carried out on as-prepared pure compounds. Mössbauer, EPR and XANES–EXAFS spectroscopies are used to probe the iron local environment and its oxidation state. The variations of the cell parameter and the solubility limit have been determined from Le-Bail refinement of XRD data. TEM analysis allowed for identification of various shapes of the single nano-crystalline $\text{Ce}_{1-x}\text{Fe}_x\text{O}_{2-x/2}$. Finally, as a function of synthesis routes, TGA measurements under Ar/5% H_2 of $\text{Ce}_{1-x}\text{Fe}_x\text{O}_{2-x/2}$ oxides have been undertaken in order to evaluate the reducibility properties which are correlated to the structural features.

Experimental section

(a) Synthesis

(i) **Preparation of $Ce_{1-x}Fe_xO_{2-x/2}$ mixed oxides by co-precipitation (CP) in basic medium.** The solid solution was prepared for $x = 0, 0.05, 0.1, 0.15$ and 0.25 . Cerium nitrate hexahydrated $Ce(NO_3)_3 \cdot 6H_2O$ (Rhodia chemicals, 99.9%) and iron nitrate nonahydrated $Fe(NO_3)_3 \cdot 9H_2O$ (Sigma Aldrich, 99.99%) were used as precursors. Stoichiometric proportions of solutions were precipitated under vigorous stirring into ammonia 0.1 M. While adding the acid precursor solution, the pH was maintained close to 10 using concentrated NH_4OH (12.3 M) and then left under stirring for 2 hours. The precipitated oxides or oxy-hydroxides were then washed with 100 ml distilled water and centrifuged (5000 rpm), three times. The precipitate was then dried overnight in an oven at $100^\circ C$ and finally annealed for 5 hours at $600^\circ C$.

(ii) **preparation of $Ce_{1-x}Fe_xO_{2-x/2}$ mixed oxides using the microwave-assisted (MW) route.** The solid solution was prepared for $x = 0, 0.05, 0.1, 0.15$ and 0.17 . The same precursors (around 20 ml of the precursor solution) were used and were precipitated in a highly basic medium composed of sodium hydroxide (around 25 ml of NaOH solution, 35% weight) and ammonia (around 3 ml of NH_4OH solution, 25% weight) with a $n_{base}/n_{cations}$ molar ratio equal to 175. The molar ratio $[NaOH]/[NH_4OH]$ was equal to 1.8. The solution (40–50 ml) containing precipitated oxides and oxy-hydroxides was then incorporated into a closed Teflon vessel (120 ml), heated up to $200^\circ C$ for 40 min using the microwave system (CEM, MARS) operated at 2450 MHz and then cooled at room temperature. A self-generated pressure of 20 bars was induced by the increase of temperature inside the Teflon container. The precipitate so obtained was finally centrifuged at 5000 rpm and washed three times with 100 ml of distilled water and dried overnight.

In the first step, the process of hydrolysis, oxidation and nucleation in the basic medium of $Ce(OH)_3$ occur in CP and MW syntheses and involve the formation of complexes with water and hydroxyls molecules such as $[Ce(OH)_x(H_2O)_y]^{(4-x)+}$ where $x + y$ is the coordination number of Ce^{4+} . In the second step, condensation processes take place with the formation of $CeO_2 \cdot nH_2O$. This latter stage differs greatly depending on the chosen synthesis route.

The microwave-assisted route leads to fast and homogenous nucleation due to important interactions between the molecules where ionic and dipolar polarizations contribute to heating. Then, heating at the core of the polar molecules leads to the formation of nanocrystalline $Ce_{1-x}Fe_xO_{2-x/2}$ with defined shapes. In the case of the classical coprecipitation route further annealing at $600^\circ C$ was performed in order to eliminate residual nitrates. Only the thermodynamically stable form corresponding to polyhedral nanocrystals was obtained after CP synthesis and annealing at $T = 600^\circ C$.

Cation ratios were checked for both synthesis routes using the ICP-OES (Inductively Coupled Plasma Spectroscopy) technique and found to be in the right chemical composition. The samples were firstly dissolved using hydrochloric acid and

heated at $T = 200^\circ C$ for 15 min using a microwave digestion system (CEM, MARS).

(b) XRD and XAFS experiments

Powder X-ray diffraction patterns were recorded on a PANalytical X'Pert MPD apparatus equipped with a Ge(111) Cu $K\alpha$ monochromator ($\lambda = 1.54059 \text{ \AA}$) and an X'Celerator detector. Data were collected over a range of $10\text{--}110^\circ$ with 0.017° steps. The lattice parameters and crystallite sizes were determined by profile matching (Le-Bail fit) using the Thomson–Cox–Hastings function implemented in the Fullprof program package.⁴⁰ X-ray absorption experiments (XANES and EXAFS) at the Fe K-edge (7112 eV) were carried out for compounds obtained by the microwave-assisted route. Data were collected at room temperature on station BM23 (upgrade of BM29 (ref. 41)) at ESRF-Grenoble-France in uniform filling operation modes. The beam was monochromatized by using a Si (111) double crystal monochromator and harmonics rejection was assured by using a Si double mirror. Spectra were recorded in fluorescence mode using a 13 monolithic Ge elements detector.

Further experiment collected at $T = 20 \text{ K}$ with a helium cryostat was performed using SAMBA beamline⁴² at SOLEIL-Saclay-France. The beamline is equipped with a sagittal focusing Si(111) monochromator and a 13 monolithic Ge elements detector. EXAFS spectra at the Fe K-edge (7112 eV) were reduced to normalized XAFS $\chi(k)$ using Ifeffit software.⁴³

Least squares analysis against the model environment was calculated and compared with hematite $\alpha\text{-Fe}_2O_3$ and magnetite $\gamma\text{-Fe}_2O_3$. Only the first shell can be refined and leads to the determination of 3 parameters, the radial Fe–O bond distance, the $2\sigma^2$ Debye–Waller factor and the zero energy shift. As far as the second shells are concerned and especially the Fe–Ce interactions, it is impossible to conclude about the occurrence of such local environments because of the too low signal/noise ratio. The results are compared with the XRD analysis and have been reported in Table 3.

(c) BET measurements

Surface areas were determined using Brunauer–Emmet–Teller (BET) calculations on isotherms recorded with an Autosorb-1 apparatus from Quantochrome Instruments. Outgassing temperatures were set at $150^\circ C$ for MW samples and $300^\circ C$ for CP ones.

(d) EPR and Mössbauer measurements

Electron paramagnetic resonance spectra were recorded at $T = 5 \text{ K}$ with a Bruker EMX spectrometer at X-band frequency (9.45 GHz) in order to identify the Fe^{3+} local environments. The WinEPR and SIMFONIA program were used to simulate and quantify the detected EPR spectra.

Mössbauer measurements were performed with a constant acceleration Halder-type spectrometer using a room temperature ^{57}Co source (Rh matrix) in the transmission geometry. The polycrystalline absorbers containing about 10 mg cm^{-2} of iron were used to avoid the experimental widening of the peaks. The velocity was calibrated using pure iron metal as the standard material.

At 293 K, a preliminary refinement using Lorentzian profile lines has shown that the spectrum consists of two doublets assigned to two sites of Fe^{3+} . Nevertheless, large values of the line width implied the existence of distributions of quadrupole splitting. Thus, a second calculation using quadrupole splitting distributions has been realized. For that, the value of the half height width was fixed at 0.30 mm s^{-1} and the isomer shift values are those determined from the first calculation.

(e) TGA analyses

Thermogravimetric analyses (TGA) were carried out in a controlled reducing atmosphere composed of 95% of argon and 5% of H_2 on a Seteram thermal analyzer. The weight losses *versus* temperature were recorded at a $5 \text{ }^\circ\text{C min}^{-1}$ heating rate from room temperature to $700 \text{ }^\circ\text{C}$. One should notice that pure ceria prepared by the MW route exhibit a higher surface area than ceria obtained by the CP-process and consequently various molecules such as H_2O and CO_2 for instance, can be adsorbed in large quantities at $T < 300\text{--}350 \text{ }^\circ\text{C}$ (identified by TGA coupled with FTIR and mass spectrometer).

(f) TEM pictures

To examine the size and the morphology of particles, transmission electron microscopy (TEM) pictures were recorded using a microscope JEOL 2200FS equipped with a field emission gun, operating at 200 kV with a point resolution of 0.23 nm. Few drops of the powder in ethanol suspension were placed on a carbon-copper grid and air-dried.

Results and discussion

(a) XRD and TEM analysis: cell parameter variations, solubility limits and morphologies

All the synthesized compounds were firstly characterized by X-ray diffraction (Fig. 1 A and B). The XRD patterns show reflections characteristic of the cubic fluorite structure of CeO_2 . The solid solution $\text{Ce}_{1-x}\text{Fe}_x\text{O}_{2-x/2}$ exists for values ranging from $x = 0$ to $x = 0.15$ and $x = 0.20$ for the microwave-assisted route and coprecipitation synthesis, respectively. Above these values, the appearance of the (110) peak characteristic of α -hematite indicates the end of solubility of iron into the CeO_2 network. For both solid solutions obtained by various synthesis routes, a shift to the higher angles was observed as the iron concentration increased. A clear decrease of the unit cell parameter *versus* Fe (x) content can be noticed (Table 1). This result is in good agreement with the substitution of a smaller cation (Fe^{3+} , 0.65 \AA , High Spin state), 6-fold coordinated to oxygen, stabilized into ceria network with oxygen vacancies, compared to Ce^{4+} (0.97 \AA) which occupies a cubic environment in the fluorite-type network. Moreover, taking into account the ionic radii of Fe^{3+} , 6-fold coordinated to oxygen and various results from the literature,^{17–20,28–36} the variations of the cell parameter appear in the right range. A linear combination of 85% of Ce–O bonds with Ce^{4+} (0.97 \AA), 8-fold coordinated to oxygen and 15% of Fe–O bond distances with Fe^{3+} (0.65 \AA), 6-fold coordinated to oxygen, leads indeed for $x = 0.15$ to a theoretical cell parameter around

5.36 \AA close to the unit-cell parameter of the compound prepared by the microwave-assisted route ($x = 0.15$, $a = 5.371 \text{ \AA}$).

However, for the same x (Fe) content the values differ as a function of synthesis routes (Fig. 2). For instance, for $x = 0.15$, the cell parameter is smaller and equal to 5.371 \AA in the case of the MW process than in the case of the CP method where $a = 5.389 \text{ \AA}$. Nevertheless, for lower Fe concentrations, the CP synthesis leads to smaller cell parameters and finally the compounds prepared by the microwave-assisted route exhibit cell parameters which vary in the largest range. These variations should be due to the nature of Fe ions substituted for Ce^{4+} one's and will be discussed in the following paragraphs.

Broadening of the peaks is also noticed as the iron concentration increases and is associated with the decrease of the crystallite sizes. In order to calculate accurate values for the microstrains and the crystallite size, the peak profiles are fitted using the pseudo-Voigt function of Thompson–Cox–Hastings⁴⁴ which allows for refining separately the angular dependence of both Lorentzian (H_L) and Gaussian (H_G) components of FWHM. As has already been observed for other solid solutions such as $\text{Ce}_{1-x}\text{Eu}_x\text{O}_{2-\delta}$ (ref. 45) or $\text{Ce}_{1-x}\text{Ca}_x\text{O}_{2-\delta}$,⁴⁶ the substitution of trivalent or divalent cations leads to a global decrease of the crystallites size or coherent domains due to the creation of constraints and oxygen vacancies in the network and the competition between surface and Madelung energies which limit the crystal growth.^{47,48} The average size of the nanoparticles determined on the basis of XRD data refinements (Table 1) decreases from a size of about 20 nm ($x = 0$) to 10 nm ($x = 0.15$) for both synthesis routes. The surface areas were determined using BET measurements (Table 1). For the MW compounds the surface area variation is in good agreement with that of refined crystallite sizes on the basis of XRD data, showing an increase in the surface area with the increase of iron concentration. The values range from $40 \text{ m}^2 \text{ g}^{-1}$ to $95 \text{ m}^2 \text{ g}^{-1}$. In the case of CP compounds surface areas vary between 20 and $60 \text{ m}^2 \text{ g}^{-1}$. Despite similar crystallite sizes – as shown by XRD analyses – the measured surface areas of CP and MW compounds are different. This can be due to annealing at $T = 600 \text{ }^\circ\text{C}$ of CP nanoparticles. Thermal treatment indeed induces the creation of sintering necks between the particles therefore decreasing the accessible surface areas. The higher surface areas found in MW compounds is consistent with the experimental procedure with fast nucleation process, relatively short synthesis durations and the absence of annealing at higher temperatures. One should notice that surface areas change drastically around $x = 0.07$ (Table 1).

The Fe solubility limit, the lattice parameter values and its variation determined for both synthesis routes cannot be explained by considering various surface areas and crystallite sizes leading to different metastable phases due to the competition between surface and Madelung energies. The lowest Fe solubility does indeed correspond to compounds prepared by the MW process with the highest surface areas. Then, the local organization of Fe and Ce cations in the fluorite network should probably explain such values and variation.

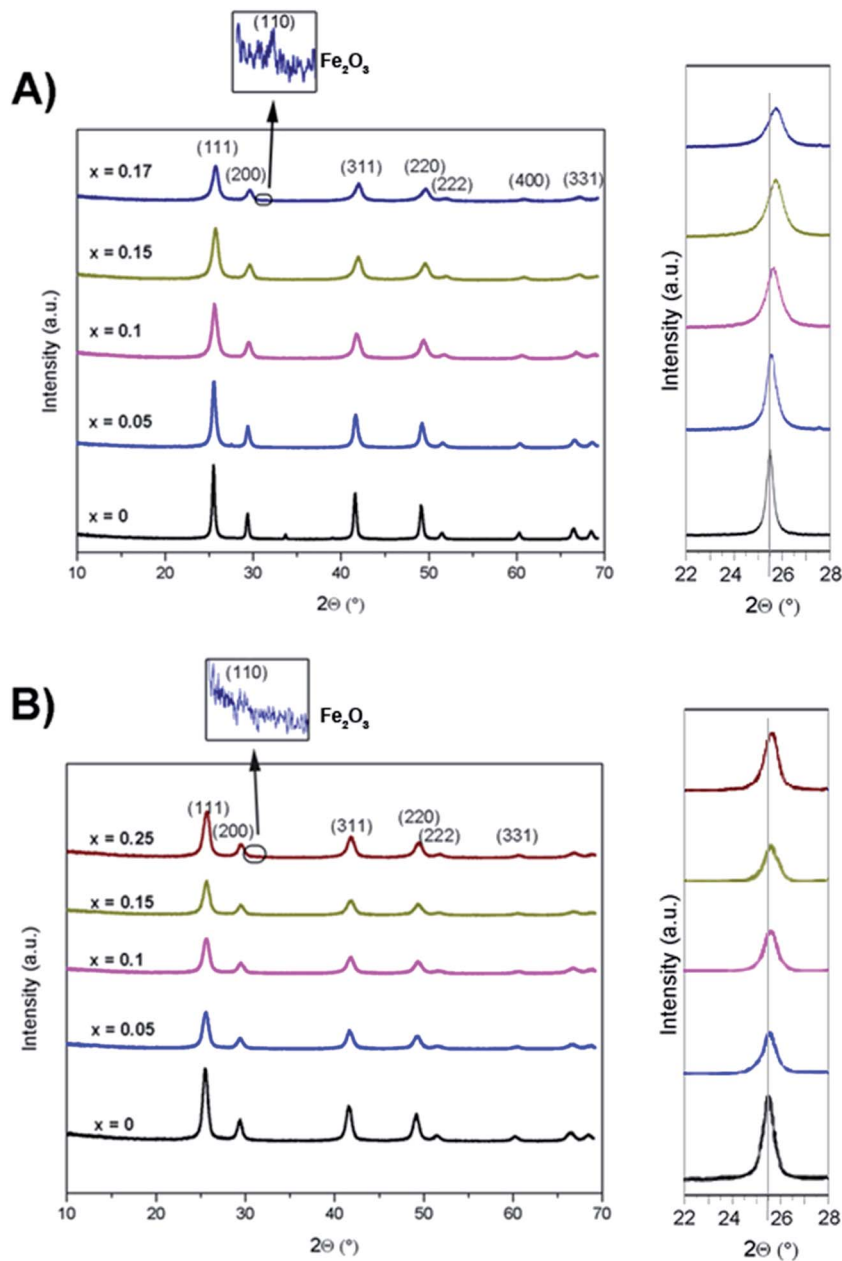


Fig. 1 XRD patterns of the $\text{Ce}_{1-x}\text{Fe}_x\text{O}_{2-x/2}$ solid solution prepared by the microwave-assisted route (A) and co-precipitation synthesis (B).

One should note that compounds prepared by the CP method followed by annealing at high temperatures exhibit polyhedral morphologies, revealing $\{111\}$ and $\{001\}$ reticular planes. In the case of the MW-assisted route, a cubic morphology with mainly the $\{001\}$ planes which are more active for reducibility than $\{111\}$ planes, is identified for the low Fe content. Furthermore, as the Fe rate increases ($x > 0.10$), a more classical polyhedral morphology appears and the surface area increases (Fig. 3).

(b) EPR, Mossbauer and XANES–EXAFS spectroscopies analyses: information about the Fe^{3+} local environment

In order to determine the iron local environments for both synthesis routes, EPR and Mössbauer spectroscopies studies

were carried out. Compounds with low iron concentrations ($0.001 \leq x \leq 0.01$) were used for the EPR analyses in order to reduce the effect of dipolar interactions and thus to increase the signal resolution. Fe^{3+} among the transition metal ions belongs to the half-filled $3d^5$ electronic configuration and exhibits ${}^6A_{1g}$ ground state with High Spin state ($S = 5/2$) and quenched orbital angular momentum ($L = 0$) under weak or intermediate crystal field. Then, the crystal field, the O–Fe charge transfer and bond covalency affect mainly the g values determined by EPR measurements.

The g values will therefore be different according to the coordination number and the symmetry of the local site. The obtained spectra (Fig. 4) can be decomposed into two parts: one centered around 350 mT for high fields and the other around 50

Table 1 Refined lattice parameters and crystallite sizes using the Fullprof software for the as-prepared compounds. Surface areas determined by the BET method are also quoted

Composition	Lattice parameter (Å)	Crystallite size (nm)	Surface area (m ² g ⁻¹)
CeO ₂ (MW)	5.413(1)	19(2)	40(4)
CeO ₂ (CP)	5.411(1)	20(2)	23(3)
Ce _{0.98} Fe _{0.02} O _{1.99} (MW)	5.408(1)	18(2)	44(5)
Ce _{0.98} Fe _{0.02} O _{1.99} (CP)	5.403(1)	9(1)	32(4)
Ce _{0.95} Fe _{0.05} O _{1.98} (MW)	5.400(1)	14(2)	58(6)
Ce _{0.95} Fe _{0.05} O _{1.98} (CP)	5.398(2)	9(1)	71(7)
Ce _{0.93} Fe _{0.07} O _{1.97} (MW)	5.392(2)	10(2)	90(9)
Ce _{0.93} Fe _{0.07} O _{1.97} (CP)	5.400(2)	14(2)	40(4)
Ce _{0.9} Fe _{0.1} O _{1.95} (MW)	5.384(2)	9(1)	91(9)
Ce _{0.9} Fe _{0.1} O _{1.95} (CP)	5.394(2)	8(1)	58(6)
Ce _{0.85} Fe _{0.15} O _{1.93} (MW)	5.371(7)	9(1)	95(10)
Ce _{0.85} Fe _{0.15} O _{1.93} (CP)	5.389(3)	9(1)	—
Ce _{0.83} Fe _{0.17} O _{1.92} (MW)	5.367(3)	9(1)	—
Ce _{0.83} Fe _{0.17} O _{1.92} (CP)	5.391(3)	9(1)	47(5)

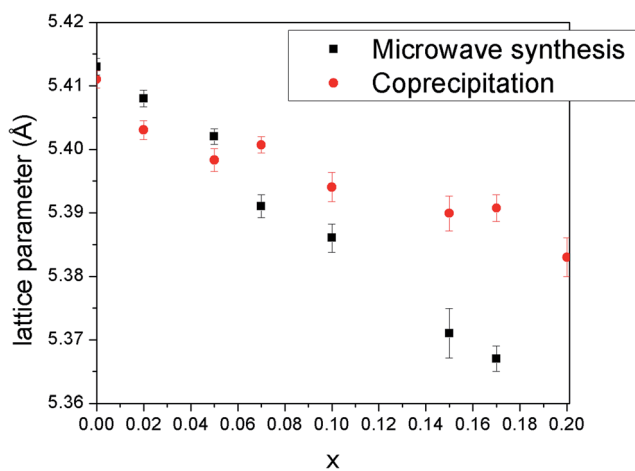


Fig. 2 Variation of the lattice parameter (Full pattern Profile Matching) versus Fe (x) content for as-prepared Ce_{1-x}Fe_xO_{2-x/2} compounds using both synthesis routes.

to 250 mT, and all these signals are unambiguously attributed to Fe³⁺.^{35,49,50}

The variation of the EPR spectra between 5 K and room temperature allows for assigning the spectrum features to three different iron environments, the first two corresponding to isolated Fe³⁺ (labelled in Fig. 4 as Fe-A and Fe-B, respectively) and the last to cluster species (labelled in Fig. 4 as Fe-C). The first site (Fe-A) is ascribed to high *g* values at 3.9, 4.3 and 7.9 (*g*₁, *g*₂ and *g*₃, respectively), corresponding to the low field region and Fe³⁺ in an isolated octahedral site with an orthorhombic distortion. This distorted octahedral environment could be associated with C_{2v} point group with 3 different Fe–O bond distances. We have also observed a less intense axial signal (Fe-B) with *g* values *g*_{||} = 5.8 and *g*_⊥ ~ 2, which is due to Fe³⁺ ions located in distorted octahedral sites with axial distortion.⁴⁹ In this case, the local symmetry could be D_{3h}, with six equal Fe–O bond distances.

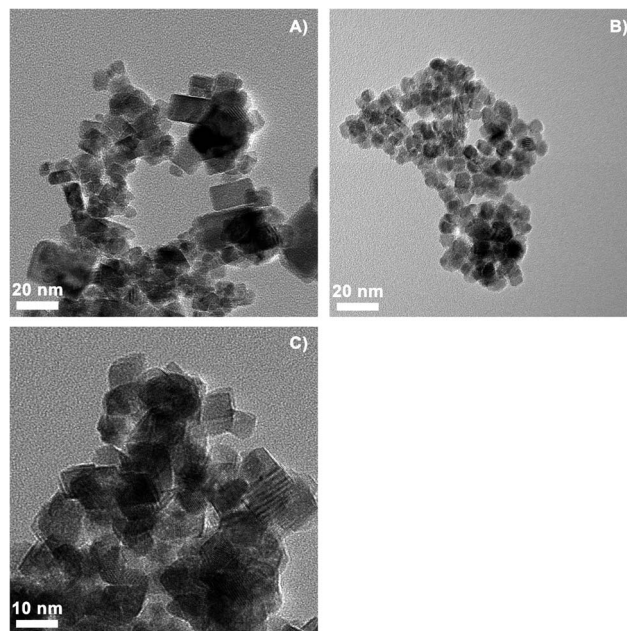


Fig. 3 HRTEM micrographs of MW nano-cubes (5% and 15% Fe content, A and B respectively) and CP nano-polyhedra (15% Fe content, C).

Both these distorted octahedral sites can be identified in bixbyite (Fe,Mn)O₃ (ref. 14 and 51) with *Ia* $\bar{3}$ space group which has derived from *Fm* $\bar{3}m$ space group of the fluorite-type network. The first site is surrounded by three kinds of Fe–O bond distances, from 1.93 Å to 2.15 Å, forming a distorted octahedron with C_{2v} point group whereas for the second site six equal Fe–O bond distances at around 2.0 Å associated with a flattened octahedral site corresponding to the D_{3h} symmetry.⁵¹

In addition to these two signals associated with isolated Fe³⁺ ions in distorted octahedral sites, a broad (about 10 mT) and intense line was observed at *g* ~ 2 (signal C). This last signal may be attributed to clusters of Fe³⁺ coupled with strong spin-spin interactions.⁵² Its position and width which mainly depend on dipole-dipole and exchange interactions remain unchanged as the temperature decreases and whatever the Fe concentration is (0.001 ≤ *x* ≤ 0.01), whereas its intensity increases with the *x* Fe content. Thus the size of Fe clusters remains the same but its amount increases with the Fe concentration (Fig. 5). *a*(Fe³⁺) values represent the normalized areas under the two main regions at low (*g* = 7.9–3.9) and high fields (*g* = 2). The different *a* values (Fig. 4a and b) associated with isolated Fe³⁺ in octahedral coordination or with Fe³⁺ clusters lead to conclude that the relative concentration of clusters is higher in the case of CP compounds compared to MW ones. These Fe³⁺ clusters are localized in the ceria network on the basis of the Fe K-edge XANES analysis presented in the following section (see below).

It should be noticed that EPR spectra show, even at room temperature, a weak axial signal D (Fig. 5) with *g* values *g*_⊥ = 1.964 and *g*_{||} = 1.942. The assignment of this signal, which was observed in many ceria-containing materials, remains unclear. It has been assigned to either unpaired electrons trapped in oxygen vacancies (stabilized by impurities or

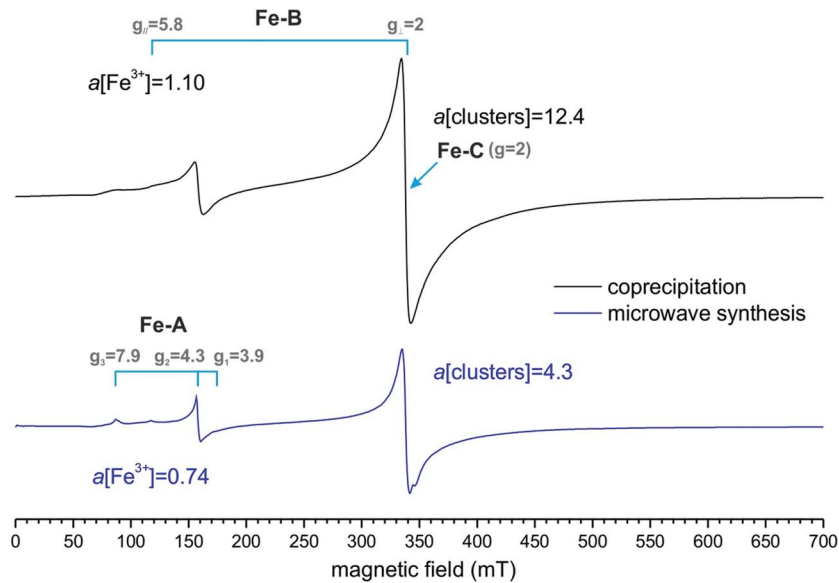


Fig. 4 Experimental X-band EPR spectra recorded at 5 K of $\text{Ce}_{0.9975}\text{Fe}_{0.0025}\text{O}_{2-\delta}$ compounds prepared by both synthesis routes (microwave frequency $\nu = 9.45$ GHz, microwave power $P = 10$ mW, amplitude of magnetic field modulation $MA = 0.6$ mT, modulation frequency $MF = 100$ kHz, spectral resolution $SR = 0.5$ mT pt^{-1}). The $a[\text{Fe}^{3+}$ or clusters] integrated area of each zone corresponding to Fe^{3+} isolated ions and Fe clusters are quoted.

structural defects) or delocalized among ions in the direct vicinity of these vacancies⁵³ or Ce^{3+} ions in low symmetry sites within the CeO_2 network.⁵⁴ However, 4f electrons associated with rare earths and Ce^{3+} can be detected by EPR only at $T < 20$ K because of their short relaxation times. In this case, local magnetic interactions with Fe^{3+} ions and high distortions of Ce^{3+} sites would increase the relaxation time and then allow detection of the Ce^{3+} EPR signal even at room

temperature. Furthermore, the concentration of Ce^{3+} paramagnetic species remains low in these samples and does not affect the reducibility properties^{53,54}

For low Fe^{3+} content, EPR analyses show that the local organization of Fe^{3+} is strongly dependent on the synthesis route. In order to confirm such tendency for higher Fe^{3+} concentrations, Mössbauer spectroscopy investigations have been performed.

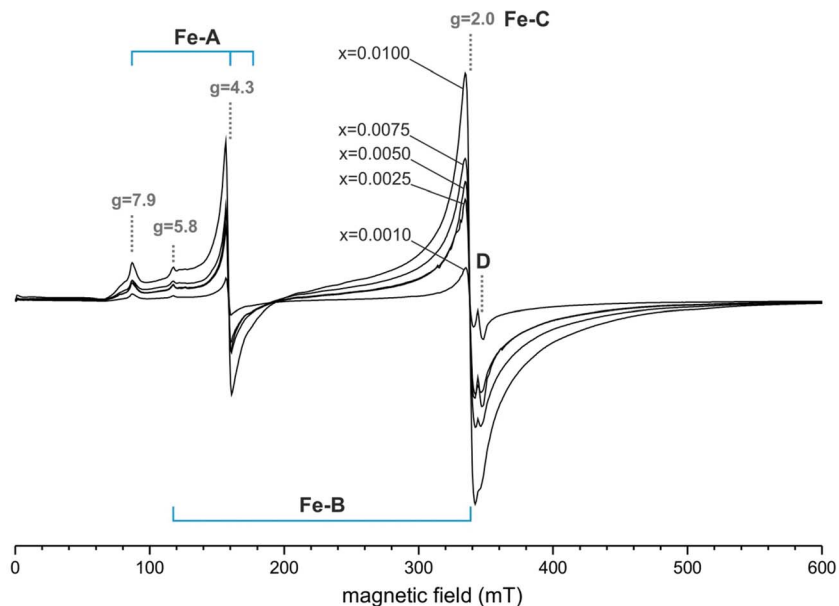


Fig. 5 Experimental X-band EPR spectra recorded at $T = 5$ K of $\text{Ce}_{1-x}\text{Fe}_x\text{O}_{2-x/2}$ compounds prepared by the MW-assisted route for various low Fe x contents ($0.001 < x < 0.01$).

Mössbauer spectroscopy analyses were carried out on $\text{Ce}_{0.9}\text{Fe}_{0.1}\text{O}_{1.95}$ compounds synthesized using both procedures (Fig. 6). No trace of magnetic $\alpha\text{-Fe}_2\text{O}_3$ was found on the basis of Mössbauer spectroscopy experiments performed at high velocities with a detection limit lower than 1% but this cannot rule out the occurrence of small $\alpha\text{-Fe}_2\text{O}_3$ clusters. For both the samples, the Mössbauer spectra, recorded at room temperature reveal two octahedral Fe^{3+} components where the proportion depends on the synthesis route (Table 2). The isomer shifts δ vary between 0.30 and 0.38 mm s^{-1} with two extreme values around 0.30 and 0.38 mm s^{-1} associated with the two components with various distributions of quadrupole splitting. The higher the isomer shift, the more ionic the chemical bonding. Then, the lowest isomer shifts could be associated with the most covalent Fe–O bonding mainly attributed to Fe^{3+} clusters. The other component with an isomer shift around 0.38 mm s^{-1} could be mostly associated with isolated Fe^{3+} octahedral sites. Moreover the average quadrupole splitting Δ based on the distribution of quadrupole splitting is slightly higher for the

first site and consequently related to a more distorted octahedral site. Taking into account the various values of the isomer shifts and quadrupole splittings as well as the content of each component, it is then possible to assign these signals. The first site corresponds to Fe^{3+} in clusters with more covalent Fe–O bonds and stronger distortions while the second site is mainly associated with isolated Fe^{3+} with more ionic Fe–O bonds where the site distortion is less pronounced. Finally, because of these values and the distribution of each component, compounds prepared by CP-route seem to exhibit a higher content of Fe^{3+} clusters in good agreement with EPR measurements performed on samples with low Fe^{3+} content.

The Fe–K edge XANES spectra (recorded at room temperature) of the $\text{Ce}_{1-x}\text{Fe}_x\text{O}_{2-x/2}$ solid solution with $x = 0.05, 0.1, 0.15$ and 0.17 prepared by the MW-assisted route are shown in Fig. 7. The Fe K-edge XANES spectra and Fourier transforms of EXAFS oscillations (recorded at $T = 20$ K) of $\text{Ce}_{0.9}\text{Fe}_{0.1}\text{O}_{1.95}$ oxides prepared by the CP or MW-assisted route have been compared with α -hematite Fe_2O_3 in Fig. 8a and b. Fe K-edge XAS data

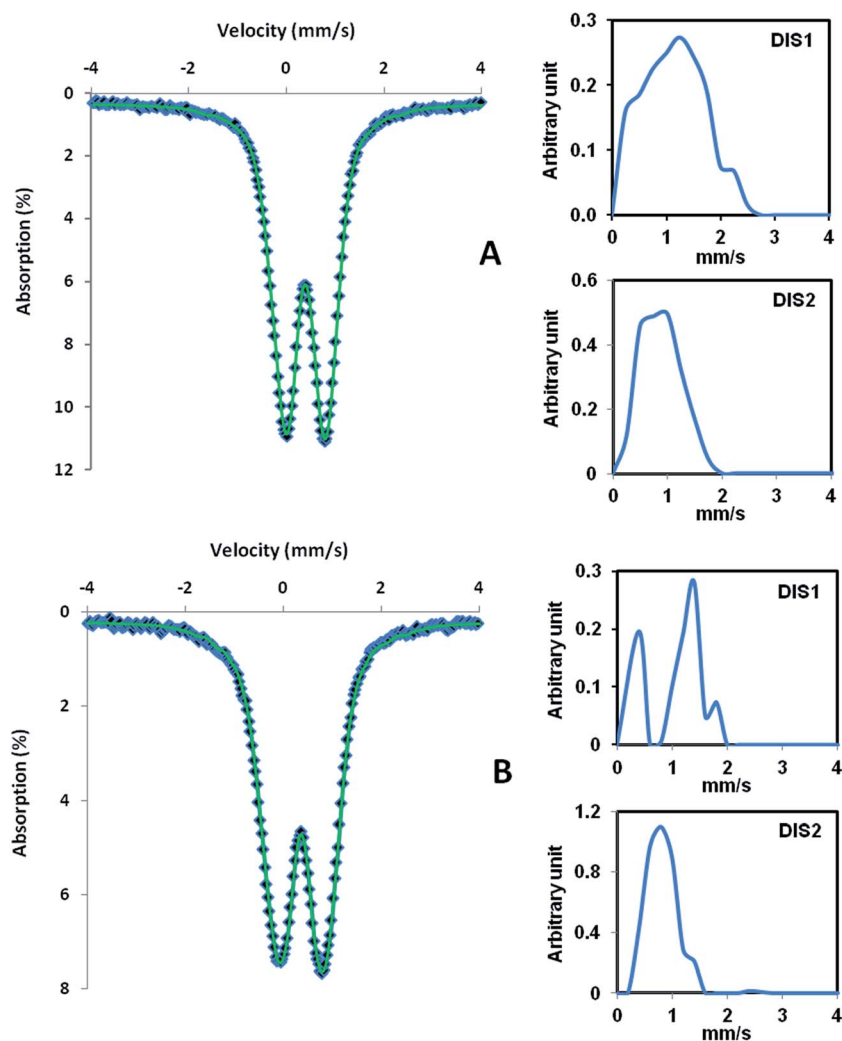


Fig. 6 Mössbauer spectra collected at room temperature for $\text{Ce}_{0.9}\text{Fe}_{0.1}\text{O}_{1.95}$ compounds prepared by (A) MW and (B) CP synthesis routes. Dotted and solid lines are the experimental and fitted data using the parameters in Table 2, respectively. Distributions of quadrupole splitting for the two sites are shown in the insets.

Table 2 Refined Mössbauer parameters for as-prepared compounds: δ : isomer shift; Γ : full width at half maximum; Δ : average quadrupole splitting on the basis of a distribution and relative abundance for each component D1 and D2

Composition	DIS	δ (mm s ⁻¹)	Γ (mm s ⁻¹)	Δ (mm s ⁻¹)	Relative abundance %
Ce _{0.9} Fe _{0.1} O _{1.95} (MW)	D1	0.33(1)	0.30	1.23(1)	21 ± 3
	D2	0.38(1)	0.30	0.83(1)	79 ± 3
Ce _{0.9} Fe _{0.1} O _{1.95} (CP)	D1	0.30(1)	0.30	1.17(1)	47 ± 3
	D2	0.37(1)	0.30	0.99(1)	53 ± 3

acquisition at $T = 20$ K allows for limiting the atomic thermal displacements and Debye–Waller factors. The Fe K-edge XANES spectra can generally be split into two regions. A pre-edge consisting of low intensity Fe 1s \rightarrow 3d quadrupole transitions appearing between 7110 and 7120 eV which are actually partially dipole allowed transitions due to 3d–4p mixing of Fe³⁺ and 3d–2p mixing between oxygen and transition metal. Owing to the overlap of Fe³⁺-3d and 4p states through O 2p states, there is a dipolar nature to this peak, making it generally more intense than pure quadrupolar, pre-edge excitations. The main-edge region which arises from dipolar Fe 1s \rightarrow 4p excitations could be treated in the multiple scattering theoretical framework. According to previous studies⁵⁵ and comparison with the α -Fe₂O₃ spectrum^{56,57} the first peak centered around 7115 eV is associated with local excitations of 1s electrons to d levels. This pre-edge do not vary with the Fe content which means that Fe d levels are not perturbed by the increasing loading. However, this pre-edge is more intense than that observed for α -Fe₂O₃ with the same Full Width at Half Maximum. It means that the local symmetry differs from C_{3v} point group of the distorted FeO₆ octahedral environment identified for α -Fe₂O₃. Then, Fe³⁺ cations in ceria occupy more non-centrosymmetric sites than in α -Fe₂O₃. Another feature appears at 7118 eV and results from a delocalized Fe–O–M inter-site hybrid excitation, where M is the first metal site in the coordination sphere of Fe. The intensity of

this peak is related to (i) the Fe–O–M bond angle, (ii) the Fe–O bond length and (iii) the coordination number of Fe³⁺. This peak is slightly more pronounced for the smaller Fe content corresponding to $x = 0.05$ and 0.10 prepared by the microwave-assisted solvothermal route, which means that the Fe–O–M interactions change a little bit in this series. However, in the white line region corresponding to 1s \rightarrow 4p_x, 4p_y, 4p_z transitions related to Fe³⁺ anti-bonding orbitals, clear differences can be noticed. The two intense peaks at 7130 eV and 7140 eV are well separated for the lowest Fe concentration and shift from each other as the Fe content increases. Moreover, for the same Fe rate equal to $x = 0.10$, convolution of both these white lines is observed for the compound prepared by the CP process. The

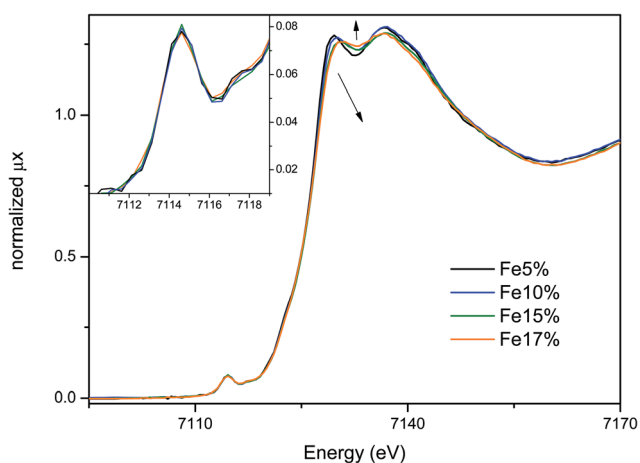


Fig. 7 Fe K-edge XANES spectra of Ce_{1-x}Fe_xO_{2-x/2} compounds with $x = 0.05, 0.1, 0.15$ and 0.17 recorded at room temperature. The inset shows the pre-edge region variation versus x between 7110 eV and 7120 eV.

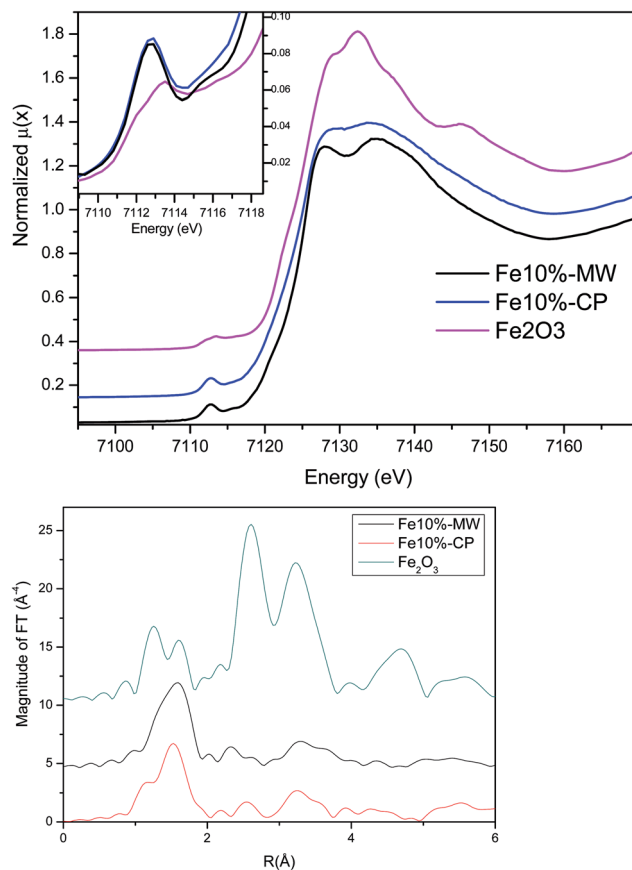


Fig. 8 Fe K-edge XANES spectra (a, above) and Fourier transforms of EXAFS oscillations (b, below) recorded at $T = 20$ K of Ce_{0.90}Fe_{0.10}O_{1.95} compounds (CP and MW-assisted routes) and α -Fe₂O₃.

comparison of these edges with α -hematite Fe_2O_3 ones show also clear difference where the white line observed for α -hematite Fe_2O_3 could have resulted from the convolution of two well separated lines identified for $\text{Ce}_{1-x}\text{Fe}_x\text{O}_{2-x/2}$ solid solutions. Furthermore, clear differences appear also on the Fourier transform of the EXAFS oscillations (Fig. 8b), for the first shell associated with the Fe–O radial distribution and the second shell related to Fe–Fe(Ce) interactions and multiple scattering phenomena. Two kinds of Fe–O bond distances appear for α - Fe_2O_3 and $\text{Ce}_{0.9}\text{Fe}_{0.1}\text{O}_{1.95}$ oxide prepared by the co-precipitation process where the Fe cluster rate seems to be high. This is not the case for $\text{Ce}_{0.9}\text{Fe}_{0.1}\text{O}_{1.95}$ oxide prepared by the microwave-assisted solvothermal route where only one but large Fe–O contribution has been identified. The intensity of the second shell for both $\text{Ce}_{0.9}\text{Fe}_{0.1}\text{O}_{1.95}$ oxides is low where the disorder is high compared to α - Fe_2O_3 . The variation of the XANES and EXAFS features with the Fe content or the synthesis route can be directly related to the occurrence of Fe–O–Fe interactions and clusters formation. Then for the MW-assisted route, the Fe cluster rate increases with the Fe concentration when CP-method is used. Furthermore, these results are in good agreement with previous EPR and Mössbauer investigations. Moreover, these Fe K-edge XANES spectra exhibit some similarities with those of doped Fe zirconia-ceria solid solution⁵⁸ or Fe-promoted sulphated zirconia samples.⁵⁹ Then, the Fe cluster and isolated Fe^{3+} in a distorted octahedral site can also be stabilized in Zr-based compounds.

Finally, the EXAFS spectra recorded at room temperature of the $\text{Ce}_{1-x}\text{Fe}_x\text{O}_{2-x/2}$ solid solution prepared by the MW-assisted route have been refined. EXAFS oscillations appear up to 10 \AA^{-1} . On the Fourier transform, only the first shell corresponding to the Fe–O bond distance has been refined and no further shells can be detected because of the low signal/noise ratio (Fig. S1 ESI,† Table 3). Then, six oxygen neighbors with an average radial bond distance around 1.98 \AA and a high Debye–Waller factor around 0.01 \AA^2 associated mainly with static disorder have been refined. These values are in good agreement with the previous analysis using various spectroscopies. However, the very short average Fe–O radial distance which is fairly compatible with Fe^{3+} , is strongly different from Ce–O ones at 2.33 \AA in Fe-doped ceria. Then, major constraints in the fluorite network have to be considered with a highly static disorder of Fe^{3+} ions randomly distributed in ceria.

(c) Discussion on the occurrence of isolated Fe^{3+} ions and Fe clusters stabilized in the ceria network

On the basis of these features and the occurrence of Fe^{3+} stabilized in clusters and isolated octahedral sites, an interpretation of the cell parameter variation and the solubility limit for both the synthesis routes can be given. The MW-assisted route allows for getting the higher concentration of Fe^{3+} isolated octahedral site, randomly distributed into the fluorite network. Each oxygen atom and anionic vacancy occupies a tetrahedral site with a random distribution of Ce^{4+} and Fe^{3+} ions on each vertex. Then, by considering a binomial law, various proportions of OCe_4 , OFeCe_3 associated with isolated Fe^{3+} cations, OFe_2Ce_2 and OFe_3Ce local environments related to Fe^{3+} clusters, can be estimated as a function of x Fe rate. The rate of each site *versus* x Fe content has been represented in Fig. S2 (ESI†) on the basis of the binomial law:

$$C_n^k = \frac{n!}{k!(n-k)!} \binom{n}{k} p^k q^{(n-k)}$$

The larger variation of the cell parameter for compounds prepared by the MW-assisted route (Fig. 2) can be associated with the higher content of isolated Fe^{3+} rate which contributes to create smaller distorted environments stabilized with oxygen vacancies and affect the global network. For the Fe cluster environment, the reorganization of oxygen and vacancies around Ce^{4+} does not have the same impact on the cell parameter and only the local environment of Ce^{4+} , close to the Fe cluster, will be affected. Then a small portion of $\text{Ce}^{4+}\text{–O}^{2-}$ bond lengths decreases in the case of the Fe^{3+} cluster and contributes to a lower reduction of the cell parameter than in the case of the isolated Fe^{3+} ion. By comparing the variations of the cell parameter for both these synthesis routes (Fig. 2), a big change seems to occur at $x = 0.07$ when the OFeCe_3 and OFe_2Ce_2 environments become non-negligible around 22.5% and 2.6%, respectively on the basis of the binomial law. At $x = 0.15$, the OFeCe_3 environment rate around 37% brings near again the OCe_4 site proportion (52%) where the OFe_2Ce_2 and OFe_3Ce total content is around 11%. Beyond this Fe rate ($x = 0.15$), the proportion of isolated Fe sites is probably too high with too much constraints in the fluorite-type network for the compounds prepared by the MW-assisted route. At $x = 0.20$, the proportion of OCe_4 and OFeCe_3 sites are equal (41%) and the OFeCe_3 local environment content reaches a maximum at $x =$

Table 3 Room temperature EXAFS analysis of the first shell (Fe K-edge) for compounds prepared by the MW-assisted route. The coordination number has been fixed to 6 on the basis of previous analyses by Mossbauer and EPR spectroscopies. The zero energy shift, the Fe–O radial bond distance and the Debye–Waller factor (DW) have been refined^a

Composition	Coordination number	Radial distance (\AA)	DW factor (\AA^2)
$\text{Ce}_{0.95}\text{Fe}_{0.05}\text{O}_{1.98}$	6	1.984 ± 0.007	0.0091 ± 0.002
$\text{Ce}_{0.9}\text{Fe}_{0.1}\text{O}_{1.95}$	6	1.980 ± 0.005	0.0086 ± 0.001
$\text{Ce}_{0.85}\text{Fe}_{0.15}\text{O}_{1.93}$	6	1.975 ± 0.005	0.0081 ± 0.001
$\text{Ce}_{0.83}\text{Fe}_{0.17}\text{O}_{1.92}$	6	1.977 ± 0.006	0.0091 ± 0.001

^a Common ΔE -zero energy shift -1.54 ± 0.80 .

0.25 (42%) beyond the limit of solubility of the $\text{Ce}_{1-x}\text{Fe}_x\text{O}_{2-x/2}$ solid solution prepared by CP-process. Thus, too much constraints appear at $x = 0.25$, even with the larger concentration of the Fe cluster in the case of compounds prepared by the CP method. In the chemistry point of view, the fast microwave-assisted hydrothermal route helps in the formation of a large proportion of isolated Fe^{3+} randomly distributed around Ce^{4+} ions. By using the CP process followed by annealing at $T = 600^\circ\text{C}$, a major proportion of Fe^{3+} clusters can be identified. Then, during the synthesis, a competition occurs between the affinity of Fe^{3+} for $\text{Ce}^{3+}/\text{Ce}^{4+}$ ions because of their electronegativity difference and the capability of Fe^{3+} to create Fe–O–Fe bonds. Finally, one should note that the two isolated Fe^{3+} distorted octahedral sites can be found in bixbyite $(\text{Fe,Mn})\text{O}_3$ whose structure has derived from the fluorite-type network.

(d) Reducibility properties

Thermogravimetric analyses were carried out under a reducing atmosphere ($\text{Ar}/5\%\text{H}_2$) up to 700°C (Fig. 9). When the slope of the curves changes drastically for the Fe-substituted ceria, one can consider in a first approximation that mainly, the reductions of Fe^{3+} and Ce^{4+} occur simultaneously with the oxygen loss from the fluorite-type network. Several compounds synthesized

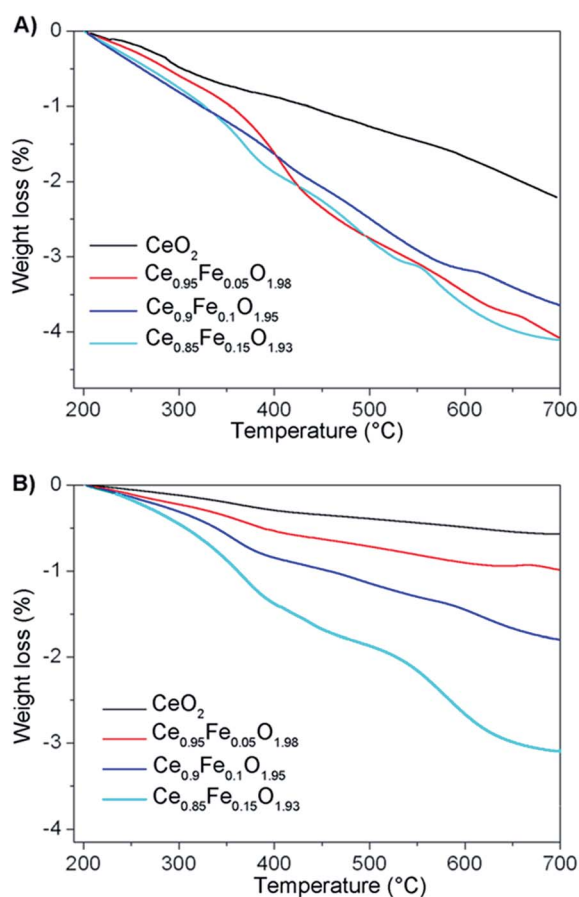


Fig. 9 TGA ($\text{Ar}/5\%\text{H}_2$) of the $\text{Ce}_{1-x}\text{Fe}_x\text{O}_{2-x/2}$ solid solution prepared by the microwave-assisted hydrothermal ($T = 200^\circ\text{C}$) route (A) and co-precipitation process followed by annealing at $T = 600^\circ\text{C}$ (B).

using CP and MW-assisted routes were analyzed. Whatever the compositions, the incorporation of iron into ceria enhances the reducibility (or the amount of reduced cations) of these compounds from both syntheses routes with a decrease of temperatures corresponding to the first reduction between $T = 300^\circ\text{C}$ and $T = 400^\circ\text{C}$. Taking into account the molar mass of the $\text{Ce}_{1-x}\text{Fe}_x\text{O}_{2-x/2}$ solid solution, a weight loss equal to 1% corresponds to 0.1 oxygen moles departure associated with 0.2 moles of reduced $\text{Ce}^{4+}/\text{Fe}^{3+}$ with the formation of 0.2 moles of $\text{Ce}^{3+}/\text{Fe}^{2+}$. The reduction process of this solid solution – leading to stabilization of metallic iron – will be described in a forthcoming paper. A maximum of weight loss at $T = 400^\circ\text{C}$ and $T = 700^\circ\text{C}$ is reached for low Fe content around $x = 0.05$ corresponding to MW-assisted compounds whereas a gradual decrease of weight loss at $T = 400^\circ\text{C}$ and $T = 700^\circ\text{C}$ versus x Fe rate can be noted for CP-compounds. For MW-assisted compounds, as previously shown, the rate of Fe^{3+} stabilized in isolated distorted octahedral sites remains high for low Fe content and the impact on Ce^{4+} first neighbors with distorted environments and their reduction rate will be high and reaches a maximum for low Fe content. This maximum is around $x = 0.05$ – 0.07 . Moreover, the occurrence of nano-cubes with $\{001\}$ faces for the low Fe rate should also explain the better reducibility of these compounds. The competition between the formation of nano-polyhedra with less exposed $\{001\}$ planes and the higher surface areas as the Fe rate increases, tends also to stabilize the content of reduced species as the Fe amount increases starting at $x > 0.05$. For instance, the MW-assisted CeO_2 and $\text{Ce}_{0.95}\text{Fe}_{0.05}\text{O}_{1.97}$ compounds with cubic shapes and comparable surface areas exhibit 30% and 60% reducibility rates ($\text{Ce}^{4+}/\text{Fe}^{3+}$ ions reduced to $\text{Ce}^{3+}/\text{Fe}^{2+}$ ones), respectively (1.5% and 3% weight loss associated with oxygen departure, respectively) at $T = 550^\circ\text{C}$. Then, just a 5% doping of a major quantity of isolated Fe^{3+} into ceria contributes to double the reducibility rate of these materials prepared by the MW-assisted route. The larger proportion of isolated Fe^{3+} ions stabilized in ceria contributes to create more ionic bonds around $\text{Ce}^{4+}/\text{Fe}^{3+}$ with a higher oxygen mobility than in the case of Fe^{3+} clusters where the covalency of the metal–oxygen bond around Fe^{3+} increases. Consequently, the reduction rate is larger as the proportion of isolated Fe^{3+} ions in ceria increases. Beyond $x = 0.05$ – 0.07 , the proportion of isolated Fe^{3+} remains high but does not strongly change and the reducibility properties are almost the same irrespective of the x Fe content. Furthermore, one should notice that compounds with a lower Ce amount and a higher Fe rate ($x = 0.15$), exhibit also the maximum reduction rate which appears at a lower temperature around $T = 300^\circ\text{C}$. In this temperature range, a forthcoming paper⁶⁰ will show that Ce^{4+} and Fe^{3+} ions are simultaneously reduced.

As far as the $\text{Ce}_{1-x}\text{Fe}_x\text{O}_{2-x/2}$ solid solution prepared by the CP method followed by annealing at $T = 600^\circ\text{C}$ is concerned, because the proportion of Fe^{3+} clusters is dominant through this synthesis route, fewer Ce^{4+} are affected by Fe^{3+} local distortions. Furthermore, the oxygen mobility and the reduction of metallic cations when Fe clusters are the dominant species, are lower because of the reorganization of the oxygen network around Ce^{4+} and the location of oxygen vacancies

around Fe clusters. A higher Fe content is necessary for this synthesis route in order to reach a high Fe clusters content which can affect a maximum of Ce^{4+} reduced ions. Then, as the Fe content rises, a gradual increase of the reduction rate is observed due to the progressive distribution of Fe clusters into ceria through this synthesis route. For $x = 0.15$, the weight loss is around 2% at $T = 550\text{ }^\circ\text{C}$ with an approximated reducibility rate of 40% ($\text{Ce}^{4+}/\text{Fe}^{3+}$ ions reduced to $\text{Ce}^{3+}/\text{Fe}^{2+}$ ones).

Conclusions

In order to prepare the $\text{Ce}_{1-x}\text{Fe}_x\text{O}_{2-x/2}$ solid solution, two various routes have been used: the classical co-precipitation of Ce^{3+} and Fe^{3+} nitrates at room temperature in a basic medium (2 h maturation) followed by annealing at $T = 600\text{ }^\circ\text{C}$ under air (5 h) and the unusual microwave-assisted hydrothermal synthesis of Ce^{3+} and Fe^{3+} nitrates in a basic medium at $T = 200\text{ }^\circ\text{C}$ (40 min). Under these last conditions, kinetics effects occur and metastable phases can be stabilized. XRD, TEM and BET experiments show clear differences for both these synthesis routes. For the compounds obtained by the microwave-assisted route, the solubility limit of Fe^{3+} into ceria is smaller ($x = 0.15$ against $x = 0.20$ for CP-method) but the amplitude of the cell parameter variation is larger. By using this synthesis route, nano-cubic morphologies are obtained for low Fe^{3+} content and nano-polyhedra are stabilized for larger Fe^{3+} amounts with higher surface areas. The local Fe^{3+} environments analyzed by EPR, Mossbauer and XANES-EXAFS spectroscopies, depend also on the synthesis route and a higher content of isolated Fe^{3+} can be identified for compounds prepared by the MW-assisted route in good agreement with the larger variation of the cell parameter determined by XRD. Such isolated Fe^{3+} stabilized in distorted octahedral sites with orthorhombic and axial distortions can be identified in the $(\text{Fe},\text{Mn})\text{O}_3$ bixbyite-type structure⁴⁶ which corresponds to a superstructure of the fluorite-type network. On the basis of a binomial law and the distribution of OM_4 tetrahedra into fluorite-type network, it is interesting to note that the OFe_2Ce_2 (Fe^{3+} cluster) and OFeCe_3 (isolated Fe^{3+} ions) site proportions become non-negligible around 2% and 22%, respectively for $x = 0.07$. It is also interesting to mention at this Fe (x) rate that the surface areas change drastically for both these synthesis routes. Moreover, the distribution of OM_4 tetrahedra on the basis of the binomial law, shows when the proportions of OCe_4 and OFeCe_3 sites become near or equal with the rate of OFe_2Ce_2 superior to 10%, the solubility limits of $x = 0.15$ (MW-assisted process) and $x = 0.20$ (CP method) are reached. Thus, too much constraints appear around Ce^{4+} at these Fe concentrations and lead to the formation of α -hematite Fe_2O_3 . As far as the reducibility properties are concerned, a maximum of reduction rate is reached for the low Fe content ($x = 0.05$) and compounds prepared by the MW-assisted route. The first reduction phenomenon occurs between $T = 300\text{ }^\circ\text{C}$ and $T = 400\text{ }^\circ\text{C}$ with a concomitant redox process involving Ce^{4+} and Fe^{3+} which will be discussed in a forthcoming paper.⁶⁰ Moreover, the reduction rate at $T = 550\text{ }^\circ\text{C}$ increases drastically from 30% (without Fe) to 60% (5% mol Fe). The same reduction rates for higher Fe contents can be explained by different effects not

only associated with the local impact of isolated Fe^{3+} ions on Ce^{4+} nearest neighbors but also to the morphology and surface area changes versus x Fe content. Finally, for compounds prepared by the classical CP-process, the gradual increase of the reduction rate up to $x = 0.20$ (limit of solubility) can be related to the progressive stabilization of Fe clusters which affects regularly the Ce^{4+} nearest neighbors. Furthermore, the ionic conductivity of Fe-substituted ceria will be strongly affected by the distribution of isolated Fe^{3+} cations and Fe^{3+} clusters into the fluorite-type network. This description with isolated polarizing cations and clusters stabilized in ceria or derived fluorite-type network can be extended to other transition metals such as Mn and Ti. In addition, stabilization of such local environments will strongly affect the reactivity and redox properties (Automotive Exhaust Catalysts and Photocatalysis) as well as the ionic conductivity (Solid Oxide Fuel Cell) or magnetic interactions (Spintronic applications).

Acknowledgements

The authors would like to thank Region Aquitaine for the financial support and the CREMEM-University of Bordeaux 1 for the electron microscopy facilities.

References

- 1 M. Funabiki, T. Yamada and K. Kayano, *Catal. Today*, 1991, **10**, 33.
- 2 A. Trovarelli, *Catalysis by Ceria and Related Materials*, Imperial College Press, 2002.
- 3 P. Singh and M. S. Hedge, *Mater. Lett.*, 2008, **181**, 3248.
- 4 B. M. Reddy, G. K. Reddy, I. Ganesh and J. M. F. Ferreira, *Catal. Lett.*, 2009, **130**, 227.
- 5 S. N. Achary, S. K. Kali, N. K. Kulkarni, P. S. R. Krishna, A. B. Shinde and A. K. Tyagi, *Chem. Mater.*, 2009, **21**, 5848.
- 6 A. Bueno-Lopez, K. Krishna, M. Makkee and J. A. Moulijn, *J. Catal.*, 2005, **230**, 237.
- 7 J. R. McBride, K. C. Hass, B. D. Poindexter and W. H. Weber, *J. Appl. Phys.*, 1994, **76**, 2435.
- 8 J.-G. Li, T. Ikegami, T. Mori and T. Wada, *Chem. Mater.*, 2001, **78**, 433.
- 9 H. Yahiro, Y. Eguchi, K. Eguchi and H. Arai, *J. App. Electrochem.*, 1988, **18**, 527.
- 10 W. Y. Hernandez, M. A. Centeno, F. Romero-Sarria and J. A. Odriozola, *J. Phys. Chem. C*, 2009, **113**, 5629.
- 11 F.-Y. Wang, S. Chen and S. Cheng, *Electrochem. Commun.*, 2004, **6**, 743.
- 12 A. B. Hungria, A. Martinez-Arias, M. Fernandez-Garcia, A. Iglesias-Juez, A. Guerrerro-Luiz, J. J. Calvino, J. C. Conesa and J. Soria, *Chem. Mater.*, 2003, **15**, 4309.
- 13 M. Yoshima, T. Hirose, S. Katano, T. Suzuki, M. Kakihana and M. Yoshimura, *Phys. Rev. B: Condens. Matter Mater. Phys.*, 1995, **51**, 8434-8437.
- 14 K. A. Kuemmerle and G. Heger, *J. Solid State Chem.*, 1999, **147**, 485-500.

- 15 I. Florea, C. Feral-Martin, J. Majimel, D. Ihiawakrim, C. Hirlimann and O. Ersen, *Cryst. Growth Des.*, 2013, **13**, 1110–1121.
- 16 R. Si and M. Flytzani-Stephanopoulos, *Angew. Chem., Int. Ed.*, 2008, **47**, 2884–2887.
- 17 F. Pérez-Alonso, M. Lopes Granado, M. Ojeda, P. Terreros, S. Rojas, T. Herranz and J. L. G. Fierro, *Chem. Mater.*, 2005, **17**, 2329.
- 18 K. Li, H. Wang, Y. Wei and D. Yan, *Appl. Catal., B*, 2010, **97**, 361.
- 19 O. H. Laguna, M. A. Centeno, G. Arzamendi, L. M. Gandia, F. Romano-Sarria and J. A. Odriozola, *Catal. Today*, 2010, **157**, 150.
- 20 K. Z. Li, H. Wang and Y. G. Wei, *J. Phys. Chem. C*, 2009, **113**, 15288.
- 21 J. B. Thomson, A. R. Armstrong and P. G. Bruce, *J. Am. Chem. Soc.*, 1996, **118**, 11129–11133.
- 22 B. Tolla, A. Demourgues, O. Isnard, M. Menetrier, M. Pouchard, L. Rabardel and T. Seguelong, *J. Mater. Chem.*, 1999, **9**, 3131–3136.
- 23 L. Yue and X.-M. Zhang, *J. Alloys Compd.*, 2009, **475**, 702.
- 24 G. Dutta, U. V. Waghmare, T. Baidya, M. S. Hedge, K. R. Priolkar and P. R. Sarode, *Chem. Mater.*, 2006, **18**, 3249–3256.
- 25 X. Li, S. Wei, Z. Zhang, Y. Zhang, Q. Su and X. Gao, *Catal. Today*, 2011, **175**, 112.
- 26 P. Quaino, O. Sysgantseva, L. Siffert, F. Tielens, C. Minot and M. Calatayud, *Chem. Phys. Lett.*, 2012, **519**, 69.
- 27 S. Yabe and T. Sato, *J. Solid State Chem.*, 2003, **171**, 7.
- 28 H. Lv, H. Tu, B. Zhao, Y. Wu and K. Hu, *Solid State Ionics*, 2007, **177**, 3467.
- 29 H. Kaneko, H. Ishihara, S. Taku, Y. Naganuma, N. Hasgawa and Y. Tamaura, *J. Mater. Sci.*, 2008, **43**, 3153.
- 30 K. Li, H. Wang, Y. Wei and M. Liu, *J. Rare Earths*, 2008, **26**, 245.
- 31 E. Aneggi, C. de Leitenburg, G. Dolcetti and A. Trovarelli, *Catal. Today*, 2006, **114**, 40.
- 32 A. Gupta and A. Kumar, *Chem. Mater.*, 2009, **21**, 4880.
- 33 H. Bao, X. Chen, J. Fang, Z. Jiang and W. Huang, *Catal. Commun.*, 2008, **125**, 160.
- 34 Y. Kaminura, S. Sato, R. Takahashi, T. Sodesawa and T. Akashi, *Appl. Catal., A*, 2003, **252**, 399.
- 35 G. Li, R. L. Smith and H. Inomata, *J. Am. Chem. Soc.*, 2001, **123**, 11091.
- 36 P. Singh and M. S. Hedge, *Dalton Trans.*, 2010, **39**, 10768–10780.
- 37 Z. D. Dohcevic-Mitrovic, N. Paunovic, M. Radovic, Z. V. Popovic, B. Matovic, B. Cekic and V. Ivanovski, *Appl. Phys. Lett.*, 2010, **96**, 203104.
- 38 B. Matovic, Z. Dohcevic-Mitrovic, M. Radovic, Z. Brankovic, G. Brankovic, S. Boskovic and Z. V. Popovic, *J. Power Sources*, 2009, **193**, 146–149.
- 39 D. Michael, P. Mingos and D. R. Baghust, *Chem. Soc. Rev.*, 1997, **26**, 233.
- 40 J. Rodriguez-Carvajal, *Phys. B*, 1993, **192**, 55.
- 41 C. Prestipino, O. Mathon, R. Hino, A. Beteva and S. Pascarelli, *J. Synchrotron Radiat.*, 2011, **18**, 176–182.
- 42 S. Belin, V. Briois, A. Traverse, M. Idir, T. Moreno and M. Ribbens, *Phys. Scr.*, 2005, 980.
- 43 M. Newville, *J. Synchrotron Radiat.*, 2001, **8**, 322–324.
- 44 P. Thompson, D. E. Cox and J. B. Hastings, *J. Appl. Crystallogr.*, 1987, **20**, 79.
- 45 W. Y. Hernandez, M. A. Centeno, F. Romero-Sarria and J. A. Odriozola, *J. Phys. Chem. C*, 2009, **113**, 5629.
- 46 L. Sronek, J. Majimel, Y. Kihn, Y. Montardi, A. Tressaud, M. Feist, C. Legein, J.-Y. Buzaré, M. Body and A. Demourgues, *Chem. Mater.*, 2007, **19**, 5110.
- 47 F. Guodong, F. Changgen and Z. J. Zhao, *Rare Earth*, 2007, **25**, 42.
- 48 W. Y. Hernandez, O. H. Laguna, M. A. Centeno and J. A. Odriozola, *J. Solid State Chem.*, 2011, **184**, 3014.
- 49 R. Kumar Singh and A. Srinivasan, *J. Magn. Magn. Mater.*, 2010, **322**, 2018.
- 50 R. P. Sreekanth Chakradhar, G. Sivaramaiah, J. Lakshmana Rao and N. O. Gopal, *Spectrochim. Acta, Part A*, 2005, **62**, 51.
- 51 B. Geller, *Acta Crystallogr., Sect. B: Struct. Crystallogr. Cryst. Chem.*, 1971, **27**, 821–828.
- 52 E. A. Zhilinskaya, V. N. Lazukin, E. A. Bychkov and I. L. Likholt, *J. Non-Cryst. Solids*, 1990, **119**, 263.
- 53 A. Martinez-Arias, J. M. Coronado, J. C. Conesa and J. Soria, in *Rare Earths*, ed. R. Sáez Puche and P. Caro, Complutense, Madrid, 1997, p. 299.
- 54 E. Abi-aad, R. Bechara, J. Grimblot and A. Aboukaïs, *Chem. Mater.*, 1993, **5**, 793–797.
- 55 J. A. Sigríst, M. G. Gaultois and A. P. Grosvenor, *J. Phys. Chem. A*, 2011, **115**, 1908–1912.
- 56 W. A. Caliebe, C.-C. Kao, J. B. Hastings, M. Taguchi, A. Kotani, T. Uozumi and F. M. F. de Groot, *Phys. Rev. B: Condens. Matter Mater. Phys.*, 1998, **58**, 13452–13458.
- 57 P. Glatzel, A. Mirone, S. G. Eeckhout, M. Sikora and G. Giuli, *Phys. Rev. B: Condens. Matter Mater. Phys.*, 2008, **77**, 115133.
- 58 V. R. Mastelaro, V. Briois, D. P. F. de Souza and C. L. Silva, *J. Eur. Ceram. Soc.*, 2003, **23**, 273.
- 59 T. Yamamora, T. Tanaka, T. Tanekaka, S. Yoshida, T. Onari, Y. Takahashi, T. Kosaka and S. Hasgawa, *J. Synchrotron Radiat.*, 1999, **6**, 425.
- 60 I. Moog, C. Prestipino, S. Figueroa, J. Majimel and A. Demourgues, *J. Phys. Chem. C*, 2014, **118**, 22746–22753.